

# A multiresolution approach to discrete tomography using DART

Andrei Dabravolski, Kees Joost Batenburg, and Jan Sijbers

## Abstract

In discrete tomography, a scanned object is assumed to consist of only a few different materials. This prior knowledge can be effectively exploited by a specialized discrete reconstruction algorithm such as Discrete Algebraic Reconstruction Technique (DART) [2], which is capable of providing more accurate reconstructions from limited data compared to conventional reconstruction algorithms. However, like most iterative reconstruction algorithms, DART suffers from long computation times. To increase the computational efficiency as well as the reconstruction quality of DART, a multiresolution version of DART (MDART) is proposed, in which the reconstruction starts on a coarse grid with big pixel (voxel) size. The resulting reconstruction is then resampled on a finer grid and used as an initial point for a subsequent DART reconstruction. This process continues until the target pixel size is reached. Experiments show that MDART can provide a significant speed-up, reducing missing wedge artefacts and improving feature reconstruction in the object compared with DART being iterated for the same time, making its use with large datasets more feasible. The biggest improvement is achieved for the objects without very fine structures and for datasets where only a few projections are available, either from a full or from a limited angular range.

**Keywords:** computed tomography, DART, discrete tomography, multiresolution, prior information.

Andrei Dabrovolski, Kees Joost Batenburg, and Jan Sijbers are with iMinds-Vision Lab, University of Antwerp, Universiteitsplein 1, 2610 Wilrijk, Belgium. Kees Joost Batenburg is also with Centrum Wiskunde & Informatica (CWI), Science Park 123, 1098 XG Amsterdam, The Netherlands.

Corresponding author: Andrei Dabrovolski, tel.: +32 32652840, fax.: +32 32652245, e-mail address: andrei.dabrovolski@uantwerpen.be

# 1 Introduction

Computed tomography is a non-invasive imaging technique which is based on reconstruction of an object from a series of projection images. It has applications on all scales, ranging from 3D imaging of nanomaterials by electron microscopy to the reconstruction of electron-density maps of the solar corona [1, 3]. In many of these applications, it is highly desirable to reduce the number of projections taken, or it is even impossible to acquire many projections. In materials science, for example, reducing the number of acquired projections leads to faster imaging which allows to increase the time resolution to study the evolution of structural changes in materials induced by stress or temperature [8]. In electron tomography, the electron beam gradually damages the object, also limiting the number of projections that can be acquired [10].

A wide range of reconstruction algorithms is available. Analytical reconstruction algorithms, such as Filtered Back Projection (FBP) [4], require a large number of projections acquired from a full angular range to obtain reconstructions of acceptable quality. Iterative reconstruction algorithms, such as the Simultaneous Iterative Reconstruction Technique (SIRT) [6], allow to incorporate prior knowledge about the object into the reconstruction process to relax these requirements in the projection data. Various forms of prior knowledge about the object can be used. Sparsity of image derivative magnitude is used in a total-variation (TV) minimization algorithm to address the few-view, limited-angle and bad-bin reconstruction problems [15]. In interior tomography, prior knowledge of the grey values within a small area inside the object can lead to more clinically feasible imaging [17]. Information about the edges of the object is shown to improve the reconstruction quality in the case of the few-view problem [5]. Finally, prior knowledge about a small number of materials forming the object allows to use Discrete Algebraic Reconstruction Technique (DART),

which can yield accurate reconstructions from a small number of projections or from a small angular range [2]. In this algorithm, continuous update steps over a subset of pixels are alternated with discretization steps in which prior knowledge is added to the reconstruction. DART has been successfully applied in electron tomography [1, 20], micro-CT [18] and magnetic resonance imaging (MRI) [14]. Being an iterative reconstruction algorithm, DART suffers from long computation times which complicates its use for large datasets or for applications where computation time is crucial.

To decrease computation time or, alternatively, improve reconstruction quality achieved in a certain computation time, a new approach is proposed in which the available projection data is first reconstructed using DART on a coarse grid. The obtained reconstruction is then resampled on a grid with smaller pixels and used as a starting point for a subsequent DART reconstruction. This process is iteratively repeated until the target pixel size is reached. The proposed approach can extend the area of applicability of DART, allowing its application to large experimental datasets.

The structure of this paper is as follows. In Section 2 our approach is explained. Section 3 describes experiment setups and presents the obtained results. The approach is discussed in Section 4. Finally, conclusions are drawn in Section 5.

## 2 Motivation and approach

We will now briefly outline the basic concepts of the DART algorithm [2]. This algorithm combines iterative update steps and intensity discretization steps, where the prior knowledge of the grey levels is incorporated into the reconstruction.

A flow chart of DART is shown in Fig. 1. The algorithm starts by calculat-

ing an initial reconstruction using an algebraic reconstruction method (ARM). Although SIRT [6] is used as the ARM throughout the paper, any iterative reconstruction algorithm could have been used. This reconstruction is then segmented. Usually, only the pixels close to the object boundary can be misclassified whereas the confidence in the classification of the interior of the object and background pixels located far from the object boundary is high. Therefore all pixels are assigned to either fixed ( $F$ ) or non-fixed ( $U$ ) pixel sets. The non-fixed pixel set  $U$  contains all boundary pixels, i. e. pixels having at least one adjacent pixel with a different grey level. A randomly chosen fraction of non-boundary pixels is also added to the set of non-fixed pixels to allow the formation of new boundaries. The remaining pixels form the fixed pixel set  $F$ . Next, several ARM iterations are performed for the non-fixed pixels while keeping the values in the fixed pixels unchanged. After that a termination criterion is checked (examples of termination criteria are given later in this Section). If the criterion is not met, the reconstruction is smoothed, finishing one DART iteration. The process is iteratively repeated until a specified convergence criterion is met.

While DART has shown its efficacy in reconstruction of micro-CT [18] and electron tomography [1, 20] datasets, in some cases DART can suffer from slow convergence, leading to long computation times required to find a practically acceptable reconstruction. Figure 2b illustrates one of such cases, where DART is capable of providing an accurate reconstruction only after a long iteration process. For the same phantom, Segmented SIRT (SSIRT) converges rapidly, though yielding a reconstruction of a poor quality (Fig. 2) (the definition of the *relative number of misclassified pixels* (RNMP) and a detailed description of the experiment conditions are given in Section 3.1). Such behaviour of DART is explained by a highly inaccurate initial ARM reconstruction. Being calculated from only a few projections, the initial reconstruction often contains strong

artefacts which then require many DART iterations in order to reduce these artefacts. Therefore, improving the initial reconstruction will lead to faster convergence and smaller computation time or to more accurate reconstructions after a fixed computation time.

In [20], applying masking during the computation of the initial SIRT reconstruction significantly reduced the missing wedge artefacts in the initial reconstruction and allowed to improve the resulting DART reconstruction. This improvement was attributed to a better estimation of grey values used in DART as those grey values were calculated from the initial reconstruction. While inaccurate grey values may indeed result in inferior quality of the DART reconstructions, even correct grey values do not guarantee fast and accurate reconstructions simultaneously (Fig. 2).

The idea of the proposed multiresolution approach is to first start a DART reconstruction on a coarse reconstruction grid and then use the resampled resulting reconstruction as a starting point for a subsequent reconstruction on a finer grid (Fig. 3). The use of coarser grids makes the reconstruction problem less ill-posed as the number of unknowns decreases and the number of equations remains the same. This allows to compute a good estimation of the object and then improve it on finer grids to reveal finer structures which cannot be reconstructed on the initial coarse grid.

Since DART is a heuristic algorithm, there is no formal definition of the conditions which guarantee the convergence of the reconstruction process. The following termination criteria can be used in practice:

- a certain *number of iterations* are performed;
- the *relative number of modified pixels* is smaller than a given threshold.

If only a few pixels change their values during the iteration, the object is mainly reconstructed;

- the difference in the *projection distance* (Eq. (1)) between the reconstructions after two consecutive iterations is smaller than a given threshold. This means that the reconstruction stops improvement.

The projection distance for a reconstruction  $\mathbf{x} \in \mathbb{R}^n$  is defined as

$$D(\mathbf{x}) = \|\mathbf{Wx} - \mathbf{p}\|_2, \quad (1)$$

where  $\mathbf{W} \in \mathbb{R}^{m \times n}$  is the projection matrix and  $\mathbf{p} \in \mathbb{R}^m$  denotes the measured projection data.

In our experiments, the modified projection distance criterion was used: iterations were stopped if the criterion held for three consecutive iterations.

Let *MDART*  $q$  denote the multiresolution DART algorithm which operates on  $q$  reconstruction grids or, alternatively, performs  $q - 1$  switchings to a finer reconstruction grid, in which the pixel size is halved. This algorithm starts from the pixel size which is  $2^{q-1}$  times bigger than the target pixel size. Note that MDART 1 is then identical to the conventional DART. Figure 4 illustrates these concepts showing the reconstruction grids and the projection geometry for MDART 2. Note that detector elements and projecting rays remain unmodified allowing to use the available projection data unaltered.

## 3 Experiments

### 3.1 Noiseless simulations

A number of simulation experiments were run using phantom images to demonstrate the proposed approach. In all simulation experiments described in the paper, the size of the phantoms was  $4096 \times 4096$  pixels while reconstructions were performed on a reconstruction grid of  $1024 \times 1024$  pixels to reduce the effect of the pixelation on the reconstructions. A number of  $m$  equiangular fan beam

projections were computed from the original phantoms using Joseph's projection method [7]. A detector with  $n = 1024$  elements was used. All experiments presented in the paper were implemented using the ASTRA toolbox [13] where GPU acceleration was used extensively [12].

Four reconstruction algorithms were compared:

- Segmented SIRT (**SSIRT**). The well known SIRT reconstruction algorithm [6] was used to calculate the reconstructions which were then segmented using a global threshold for a fair comparison.
- **DART** [2]. An initial reconstruction was calculated using 50 SIRT iterations, 10 SIRT iterations were applied to the non-fixed pixels during each DART iteration.
- **MDART 4** and **MDART 2**. All parameters of the underlying DART algorithm were identical to the described above. Reconstruction resampling was performed using the bilinear interpolation.

Correct grey values and a global threshold were used in the simulation experiments. All participating algorithms were stopped after a certain iteration time. The quality of the reconstructions was assessed by calculating the *relative number of misclassified pixels* (RNMP) according to

$$RNMP(I, \tilde{I}) = \frac{\left| \{(i, j) \mid \tilde{I}(i, j) \neq I(i, j)\} \right|}{\left| \{(i, j) \mid I(i, j) > 0\} \right|}, \quad (2)$$

where  $I$  is the original phantom and  $\tilde{I}$  denotes the reconstruction resampled on the same grid as  $I$  using the nearest-neighbour interpolation.

In the first series of experiments four phantom images (Fig. 5) were used. Phantom 1 (Fig. 5a) is a disk with a number of holes of radius 100 pixels. It is identical to the phantom used in Section 2 (Fig. 2a). Phantom 2 (Fig. 5b) represents a cylinder head of an internal combustion engine, Phantom 3 (Fig. 5c)

is a Siemens star-like phantom, Phantom 4 (Fig. 5d) consists of a number of intersecting ellipses and has three grey values, whereas the former three phantoms are binary. From these phantoms, a number  $m$  equiangular projections were computed. These projections were then reconstructed using the algorithms under consideration.

The obtained results are shown in Figs. 6 and 7, which suggest that MDART can provide significantly better reconstruction quality in only a fraction of computation time compared to SSIRT and DART, especially when there are only a few projections available.

For the second series of experiments, a number of phantoms were used, each consisting of a disk with randomly placed circular holes of a particular size (Fig. 8). Three phantoms were created for each hole size. For these phantoms, projections from complete and from the limited angular ranges were computed in order to evaluate the applicability of the proposed approach for objects with features of various size and for the datasets with the missing wedge.

Figure 9 presents the obtained results after 30 s iteration time, demonstrating the average RNMP over the phantoms with the holes of the particular size together with the standard errors (shown as shaded areas in the plots). Figure 10 shows the corresponding reconstructions of one of the phantoms with holes of radius 50 pixels calculated from 20 projections with 90° missing wedge. These plots demonstrate the ability of MDART to provide reconstructions of significantly higher quality compared to SSIRT and DART and to reduce missing wedge artefacts. The biggest gain compared to DART is achieved in the experiments with bigger missing wedge and smaller number of projections. The poor performance of MDART 4 on the phantoms with the hole radii of 30 pixels is explained by the fact that on the coarsest reconstruction grid used by MDART 4 such holes have a radius of less than one pixel which complicates

their detection with a discrete reconstruction algorithm. Note that for the holes of radius 60 pixels or bigger MDART 4 shows the best results among all considered algorithms gaining from the use of coarser grids.

### 3.2 Simulations with noise

In order to evaluate the proposed multiresolution approach in a more realistic situation, Poisson noise was added to one of the experiments shown in Section 3.1. For the cylinder head phantom (Fig. 5b),  $K = 5$  noisy sets of projection data were obtained for each noise level. For each noisy projection dataset the reconstructions were built as described in Section 3.1. The mean values of  $RNMP(I, \tilde{I})$  over these  $K$  reconstructions after 25 s iteration time are shown in Fig. 11, from which we see that the proposed method can outperform SSIRT and DART even in the presence of noise. This plot also demonstrates a slightly higher MDART 4 robustness against noise compared to MDART 2.

### 3.3 Real experiments

The following experiments were conducted in order to demonstrate the performance of the proposed multiresolution approach on real data.

For the first experiment, a hardware phantom with a diameter of 70 mm was scanned using HECTOR micro-CT system developed by UGCT (the Ghent University Centre for X-ray Tomography, Belgium) in collaboration with X-Ray Engineering (XRE bvba, Ghent, Belgium) [9]. For this object, a full-angle cone-beam dataset was acquired containing 2401 projections of  $2000 \times 2000$  pixels. The source-detector distance was 1250 mm and the source-object distance was 275 mm. One slice from this dataset was reconstructed with 1000 iterations of SIRT (Fig. 12a) on a  $2000 \times 2000$  reconstruction grid with a pixel size of  $44 \mu\text{m}$ .

In the second experiment, a gypsum jaw model was scanned using a desktop

micro-CT system SkyScan-1172 (Bruker-MicroCT, Belgium). A full-angle cone-beam dataset consisting of 400 projections of  $1984 \times 524$  pixels was acquired. One slice from this dataset was reconstructed on a  $1984 \times 1984$  grid with a pixel size of  $34.7 \mu\text{m}$  using 500 SIRT iterations (Fig. 12b).

Finally, a coral was scanned on the TOMCAT beamline [16] at the Swiss Light Source, Paul Scherrer Institut (Villigen, Switzerland). A full-angle parallel-beam dataset consisting of 1001 projections of  $1022 \times 378$  pixels was acquired. One slice from this dataset was reconstructed on a  $1022 \times 1022$  grid using 500 SIRT iterations (Fig. 12c).

The reconstructions using all available projections (Fig. 12) were segmented using the Otsu segmentation algorithm [11] and used as a ground truth in the following experiments. A number of  $m$  projections of the same slice were chosen to form datasets with limited angular ranges. These datasets were then reconstructed using the algorithms described in Section 3.1. Since true grey values to be used in DART and MDART were not known, these values were estimated as mean values in each segmentation class of the Otsu segmentation of the SIRT reconstructions shown in Fig. 12.

The obtained results are presented in Figs 13 and 14. Figures 13a, 13c and 13e demonstrate the ability of MDART to significantly speed up the reconstruction process and to yield more accurate results compared to SSIRT and DART. Figures 13b, 13d and 13f confirm that MDART suffers from the missing wedge in the projection data less than other considered algorithms. Lower performance of all compared algorithms on the jaw model dataset without the missing wedge compared to the dataset with the  $30^\circ$  missing wedge (Fig. 13d) is explained by the dependency of the reconstruction quality on the actual projection directions for some objects, especially if there are only a small number of projections used [19]. Moderate performance of MDART 4 on the coral dataset (Figs. 13e and

13f) compared to the performance of DART and MDART 2 is caused by the presence of very fine details in the object, which cannot be reconstructed on the coarsest reconstruction grid used by this algorithm. Examples of the reconstructions of the hardware phantom using  $m = 20$  projections with  $90^\circ$  missing wedge shown in Fig. 14 suggest that the proposed approach, and MDART 4 in particular, can significantly reduce missing wedge artefacts and improve feature reconstruction for real objects. Therefore, experimental studies conform to the simulations described in Section 3.1, showing the ability of the proposed approach to faster yield reconstructions of superior quality compared to those produced by SSIRT and DART for real datasets.

## 4 Discussion

The proposed multiresolution DART algorithm starts reconstruction on a coarse reconstruction grid and then uses the resampled resulting reconstruction as an initial point for a new reconstruction process on a finer grid, iteratively switching to the new grid until the target pixel size is reached. In our experiments, the following pixel size was always two times smaller than the current one. A certain variation in the pixel size changing strategy can have additional benefits in terms of computation time.

Experiments show that the proposed approach allows to create accurate reconstructions significantly faster than DART. Speed-up comes from the following two facts: iteration time decreases together with the number of pixels in the reconstruction and DART converges faster when starting from a better initial reconstruction. More accurate initial reconstruction results from the fact that use of the coarse grids makes the reconstruction problem less ill-posed decreasing the number of unknowns while preserving the number of equations. This is especially important in case when the limited number of projections is

available or the projections were acquired from a limited angular range since the initial reconstruction calculated from such data can suffer from strong artefacts which sometimes slow down the convergence of conventional DART.

The choice of the starting pixel size has a significant influence on the performance of the proposed approach. On the one hand, the smaller the features present in the object, the smaller should be the starting pixel size. On the other hand, the bigger the starting pixel, the higher the potential for a speed-up and for robustness against noise. This trade-off should be made having a particular reconstruction problem in mind.

The proposed multiresolution approach can broaden the use of DART for large experimental datasets. It also allows to further decrease the number of projections required to obtain accurate reconstructions in a reasonable time.

## 5 Conclusion

We proposed the multiresolution DART algorithm for discrete tomography. This approach is based on the iterative use of a resampled reconstruction created on a coarse grid as a starting point for a subsequent reconstruction on a finer grid. Our experiments showed that the proposed approach can lead to accurate reconstructions calculated in only a fraction of time compared to DART. The biggest improvement is reached for the datasets with very small number of projections and acquired from a limited angular range. Reconstructions of the real datasets demonstrated an ability of the multiresolution DART to significantly decrease the missing wedge artefacts and improve feature reconstruction in the object compared to the conventional DART algorithm being iterated for the same time.

## 6 Acknowledgements

The authors would like to thank UGCT from the University of Ghent for the hardware phantom dataset. The authors are grateful to A. Sasov from Bruker-MicroCT and Elke Van de Casteele for their help in the data acquisition for the jaw model. The authors would also like to thank Federica Marone from Paul Scherrer Institut (Switzerland) for providing the coral dataset. This work was financially supported by the BOF LP project 25778 and the SBO project TomFood from the Agency for Innovation by Science and Technology in Flanders (IWT). K.J.B. was supported by the Netherlands Organisation for Scientific Research (NWO), programme 639.072.005.

## References

- [1] K J Batenburg, S Bals, J Sijbers, C Kuebel, P A Midgley, J C Hernandez, U Kaiser, E R Encina, E A Coronado, and G Van Tendeloo. 3D imaging of nanomaterials by discrete tomography. *Ultramicroscopy*, 109(6):730–740, May 2009.
- [2] K J Batenburg and J Sijbers. DART: A Practical Reconstruction Algorithm for Discrete Tomography. *IEEE Transactions on Image Processing*, 20(9):2542–2553, Sep 2011.
- [3] M D Butala, R J Hewett, R A Frazin, and F Kamalabadi. Dynamic Three-Dimensional Tomography of the Solar Corona. *Solar Physics*, 262(2):495–509, Apr 2010.
- [4] T M Buzug. *Computed Tomography: From Photon Statistics to Modern Cone-Beam CT*. Springer, 2008.

- [5] M Fedrigo, A Wenger, and C Hoeschen. Investigating tomographic reconstruction with a priori geometrical information. *Journal of X-Ray Science and Technology*, 20(1):1–10, 2012.
- [6] J Gregor and T Benson. Computational analysis and improvement of SIRT. *IEEE Transactions on Medical Imaging*, 27(7):918–924, Jul 2008.
- [7] P M Joseph. An improved algorithm for reprojecting rays through pixel images. *IEEE Transactions on Medical Imaging*, 1(3):192–196, 1982.
- [8] E Maire and P J Withers. Quantitative X-ray tomography. *International Materials Reviews*, 59(1):1–43, Jan 2014.
- [9] B Masschaele, M Dierick, D Van Loo, M N Boone, L Brabant, E Pauwels, V Cnudde, and L Van Hoorebeke. HECTOR: A 240kV micro-CT setup optimized for research. In *11th International Conference on X-ray Microscopy (XRM2012)*, volume 463 of *Journal of Physics Conference Series*, 2013.
- [10] P A Midgley and R E Dunin-Borkowski. Electron tomography and holography in materials science. *Nature Materials*, 8(4):271–280, Apr 2009.
- [11] N Otsu. Threshold Selection Method from Gray-Level Histograms. *IEEE Transactions on Systems, Man, and Cybernetics*, 9(1):62–66, 1979.
- [12] W J Palenstijn, K J Batenburg, and J Sijbers. Performance improvements for iterative electron tomography reconstruction using graphics processing units (GPUs). *Journal of Structural Biology*, 176(2):250–253, Nov 2011.
- [13] W J Palenstijn, K J Batenburg, and J Sijbers. The ASTRA Tomography Toolbox. In *13th International Conference on Computational and Mathematical Methods in Science and Engineering*, CMMSE 2013, 2013.

- [14] H Segers, W J Palenstijn, K J Batenburg, and J Sijbers. Discrete Tomography in MRI: a Simulation Study. *Fundamenta Informaticae*, 125(3-4):223–237, 2013.
- [15] E Y Sidky, C M Kao, and X Pan. Accurate image reconstruction from few-views and limited-angle data in divergent-beam CT. *Journal of X-Ray Science and Technology*, 14(2):119–139, 2006.
- [16] M Stampanoni, A Groso, A Isenegger, G Mikuljan, Q Chen, A Bertrand, S Henein, R Betemps, U Frommherz, P Boehler, D Meister, M Lange, and R Abela. Trends in synchrotron-based tomographic imaging: the SLS experience. In Bonse, U, editor, *Developments in X-ray Tomography V*, volume 6318 of *Proceedings of SPIE*, 2006.
- [17] S Tang, Y Yang, and X Tang. Practical interior tomography with radial Hilbert filtering and a priori knowledge in a small round area. *Journal of X-Ray Science and Technology*, 20(4):405–422, 2012.
- [18] Wim van Aarle, Kees Joost Batenburg, Gert Van Gompel, Elke Van de Casteele, and Jan Sijbers. Super-Resolution for Computed Tomography Based on Discrete Tomography. *IEEE Transactions on Image Processing*, 23(3):1181–1193, Mar 2014.
- [19] L Varga, P Balazs, and A Nagy. Direction-dependency of binary tomographic reconstruction algorithms. *Graphical Models*, 73:365–375, 2011.
- [20] A Zuerner, M Doeblinger, V Cauda, R Wei, and T Bein. Discrete tomography of demanding samples based on a modified SIRT algorithm. *Ultramicroscopy*, 115:41–49, Apr 2012.

## List of Figures

1	Flow chart of DART [2]. . . . .	20
2	Phantom, $4096 \times 4096$ pixels size, with holes of radius 100 pixels (a) and RNMP as a function of the computation time for the reconstruction of this phantom using SSIRT and DART from $m = 20$ projections (b), which demonstrate the slow convergence of DART for some datasets. Error images for SSIRT (c) and DART (d) reconstructions after 500 s iteration time. Red and green in the error images correspond to misclassified background and object pixels, respectively, black and yellow represent correctly classified background and object pixels, respectively. . . . .	21
3	Flow chart of the multiresolution DART algorithm. . . . .	22
4	Projection geometry and reconstruction grids used by MDART 2: (a) the coarse reconstruction grid and (b) the target reconstruction grid. . . . .	23
5	Phantoms 1–4 (a-d), $4096 \times 4096$ pixels. . . . .	24
6	RNMP as a function of the computation time for the reconstructions of Phantoms 1–2 (Figs. 5a and 5b) from $m$ projections (a-d). Black and grey points on the MDART curves mark the moments of switching to a finer reconstruction grid. . . . .	25
7	RNMP as a function of the computation time for the reconstructions of Phantoms 3–4 (Figs. 5c and 5d) from $m$ projections (a-d). Black and grey points on the MDART curves mark the moments of switching to a finer reconstruction grid. . . . .	26
8	Examples of the phantoms, $4096 \times 4096$ pixels size, with holes of radius 50 (a) and 80 (b) pixels used in the experiments of Section 3.1. . . . .	27

9	RNMP for the reconstructions of the phantoms with various hole sizes from $m = 20$ projections after 30 s iteration time: (a) as a function of the hole radius for the $90^\circ$ missing wedge and (b) as a function of the missing wedge for the phantoms with the hole radius of 50 pixels. . . . .	28
10	Reconstructions of the phantom with holes of radius 50 pixels of unit size after iterating for 30 s with SSIRT (a), DART (b) and MDART 2 (c) using $m = 20$ projections with $90^\circ$ missing wedge together with the corresponding error images (d-f). Red and green in the error images correspond to misclassified background and object pixels, respectively, black and yellow represent correctly classified background and object pixels, respectively. . . . .	29
11	RNMP as a function of the photon count for the reconstructions of the cylinder head phantom (Fig. 5b) from $m = 20$ projections with noise as described in Section 3.2. The iteration process was stopped after 25 s. . . . .	30
12	SIRT reconstructions of slices of the real datasets using all available projections: (a) the hardware phantom, 2401 projections, (b) the jaw model, 400 projections, (c) the coral, 1001 projections. . . . .	31
13	RNMP for the reconstructions of the real datasets (Fig. 12) as a function of the computation time from the data with the missing wedge (a, c, e) and as a function of the missing wedge after 50 s iteration time (b, d, f). Missing wedge is $90^\circ$ in (a) and (c) and $30^\circ$ in (e). Black and grey points on the MDART curves (a, c, e) mark the moments of switching to a finer reconstruction grid. . . . .	32



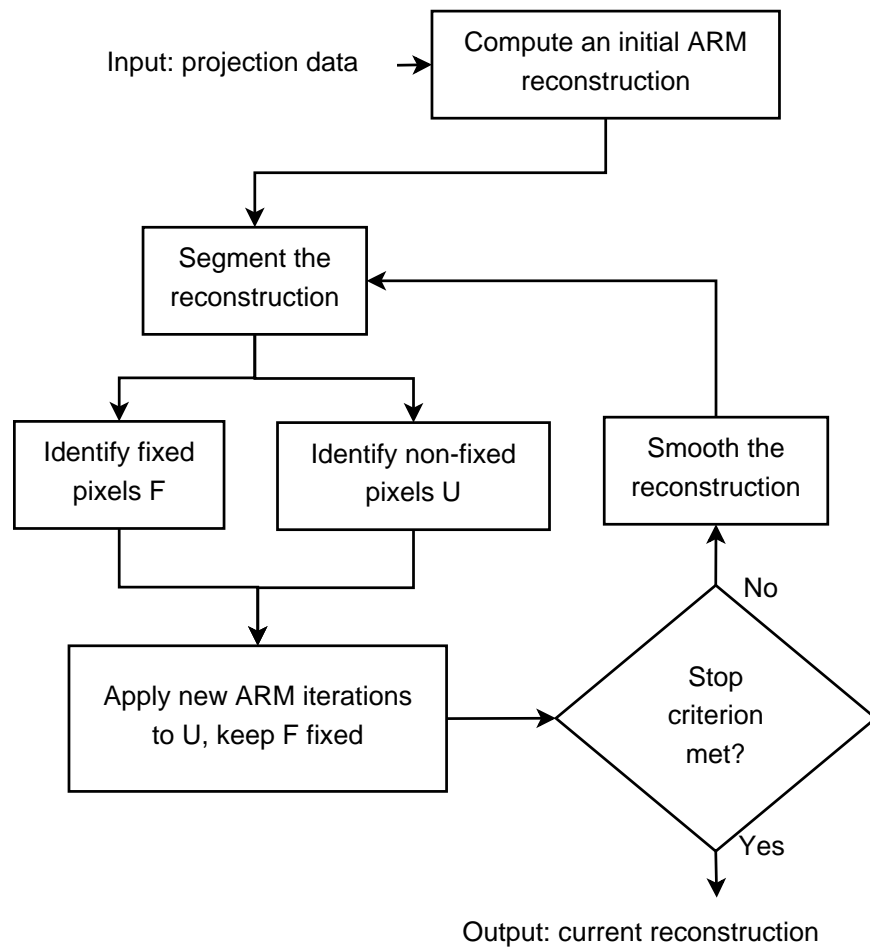


Fig. 1: Flow chart of DART [2].

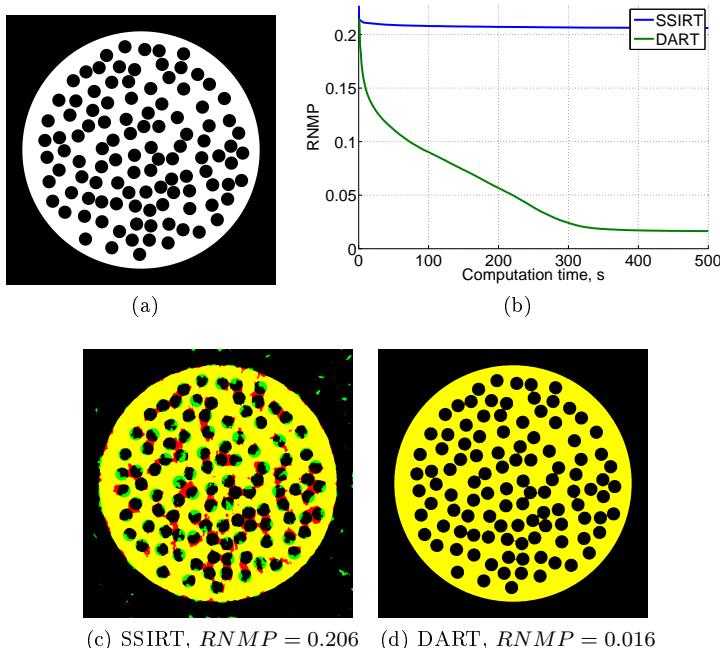


Fig. 2: Phantom,  $4096 \times 4096$  pixels size, with holes of radius 100 pixels (a) and RNMP as a function of the computation time for the reconstruction of this phantom using SSIRT and DART from  $m = 20$  projections (b), which demonstrate the slow convergence of DART for some datasets. Error images for SSIRT (c) and DART (d) reconstructions after 500 s iteration time. Red and green in the error images correspond to misclassified background and object pixels, respectively, black and yellow represent correctly classified background and object pixels, respectively.

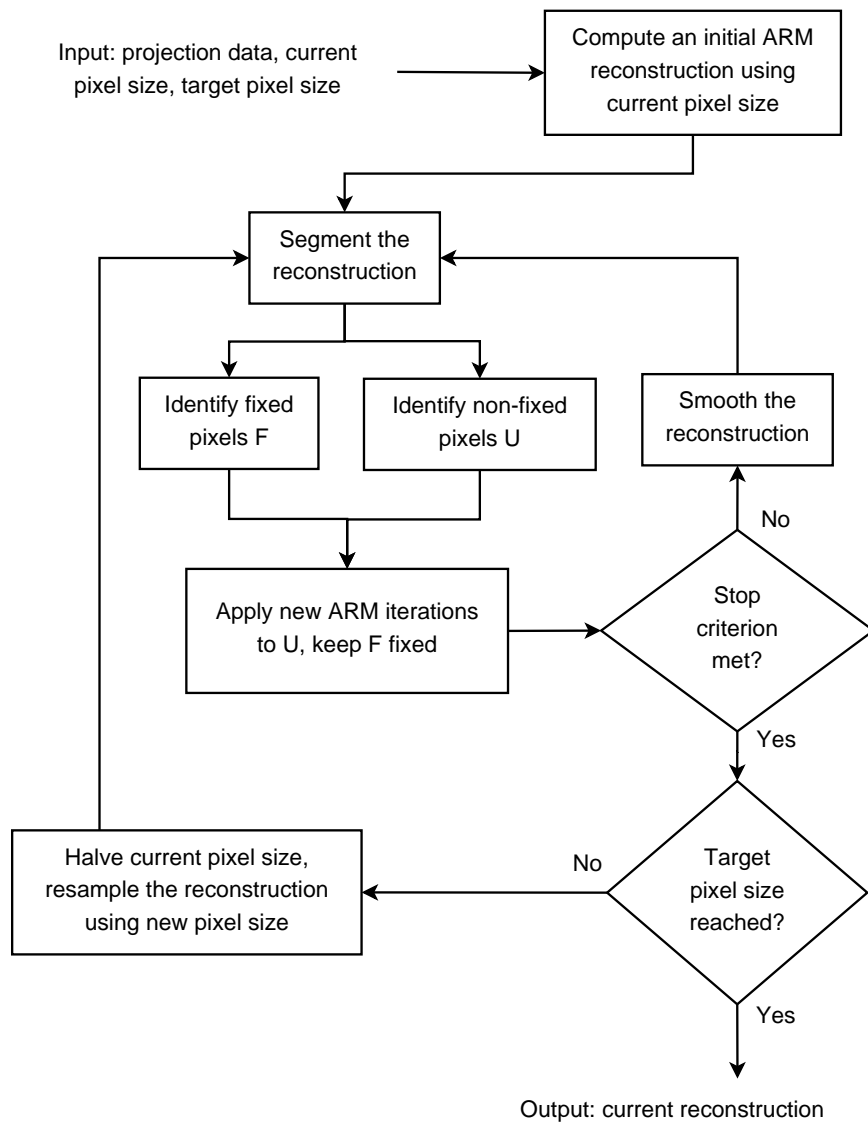


Fig. 3: Flow chart of the multiresolution DART algorithm.

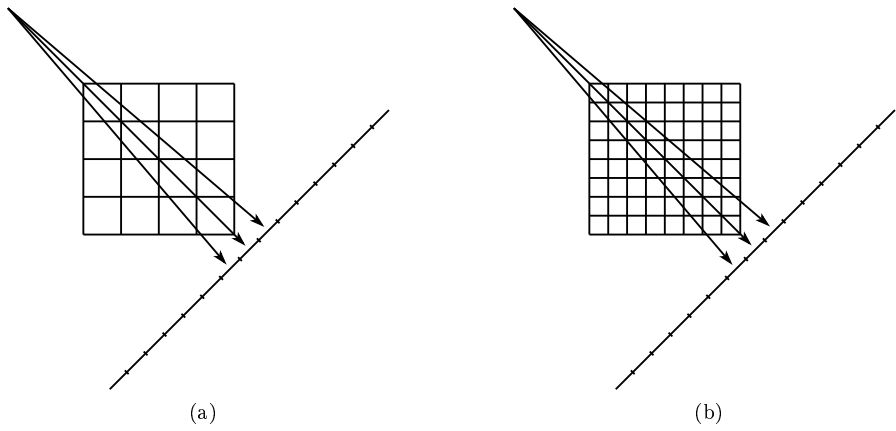


Fig. 4: Projection geometry and reconstruction grids used by MDART 2: (a) the coarse reconstruction grid and (b) the target reconstruction grid.

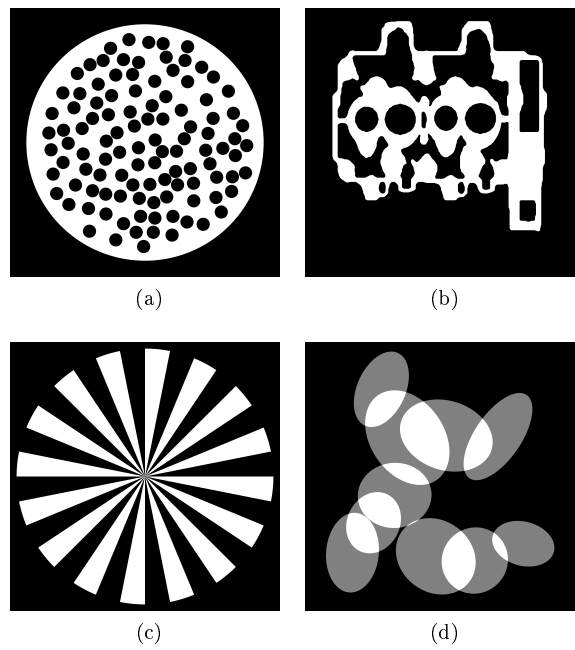


Fig. 5: Phantoms 1–4 (a-d),  $4096 \times 4096$  pixels.

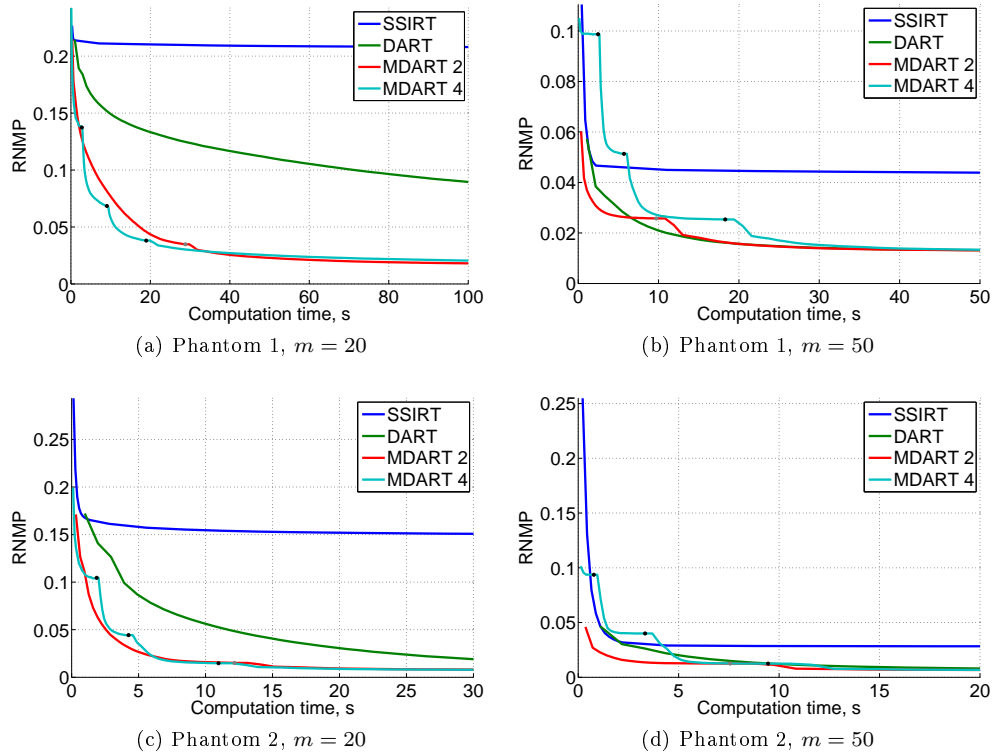


Fig. 6: RNMP as a function of the computation time for the reconstructions of Phantoms 1–2 (Figs. 5a and 5b) from  $m$  projections (a-d). Black and grey points on the MDART curves mark the moments of switching to a finer reconstruction grid.

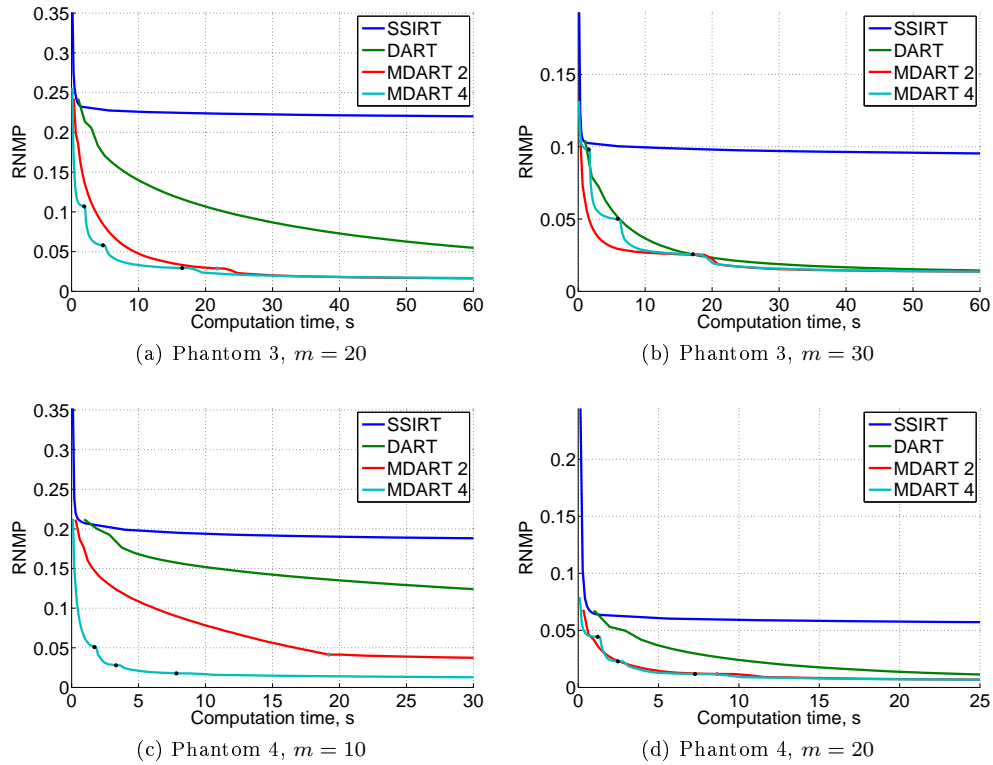


Fig. 7: RNMP as a function of the computation time for the reconstructions of Phantoms 3–4 (Figs. 5c and 5d) from  $m$  projections (a-d). Black and grey points on the MDART curves mark the moments of switching to a finer reconstruction grid.

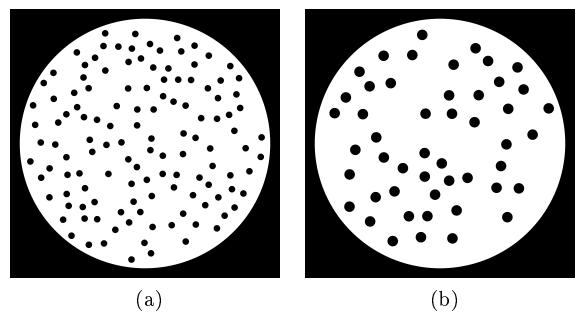


Fig. 8: Examples of the phantoms,  $4096 \times 4096$  pixels size, with holes of radius 50 (a) and 80 (b) pixels used in the experiments of Section 3.1.

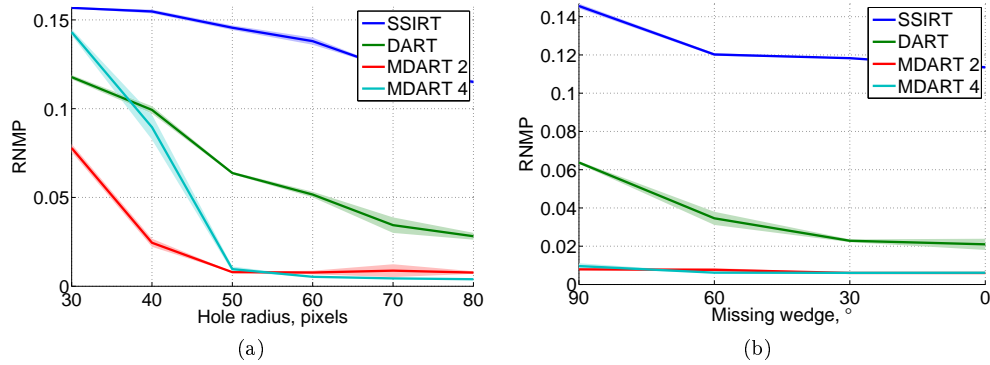


Fig. 9: RNMP for the reconstructions of the phantoms with various hole sizes from  $m = 20$  projections after 30 s iteration time: (a) as a function of the hole radius for the  $90^\circ$  missing wedge and (b) as a function of the missing wedge for the phantoms with the hole radius of 50 pixels.

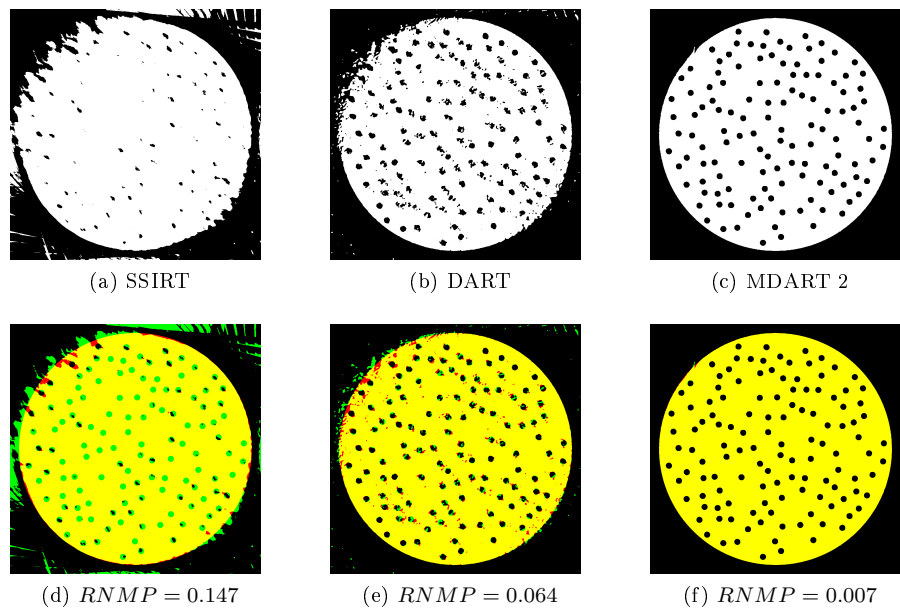


Fig. 10: Reconstructions of the phantom with holes of radius 50 pixels of unit size after iterating for 30 s with SSIRT (a), DART (b) and MDART 2 (c) using  $m = 20$  projections with  $90^\circ$  missing wedge together with the corresponding error images (d-f). Red and green in the error images correspond to misclassified background and object pixels, respectively, black and yellow represent correctly classified background and object pixels, respectively.

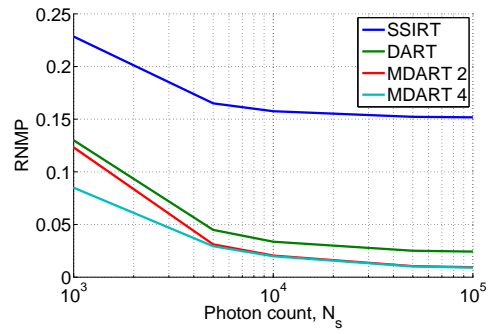


Fig. 11: RNMP as a function of the photon count for the reconstructions of the cylinder head phantom (Fig. 5b) from  $m = 20$  projections with noise as described in Section 3.2. The iteration process was stopped after 25 s.

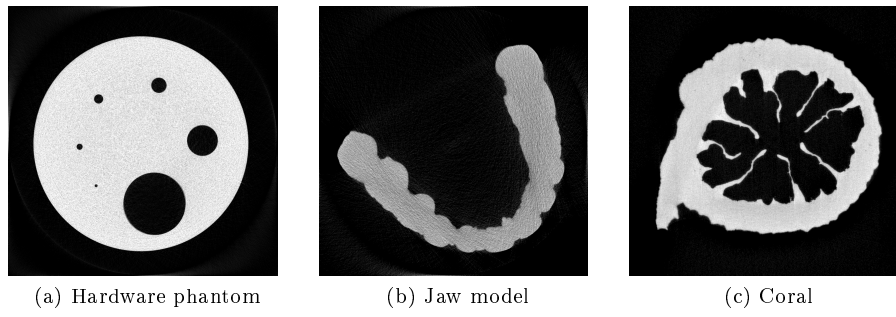


Fig. 12: SIRT reconstructions of slices of the real datasets using all available projections: (a) the hardware phantom, 2401 projections, (b) the jaw model, 400 projections, (c) the coral, 1001 projections.

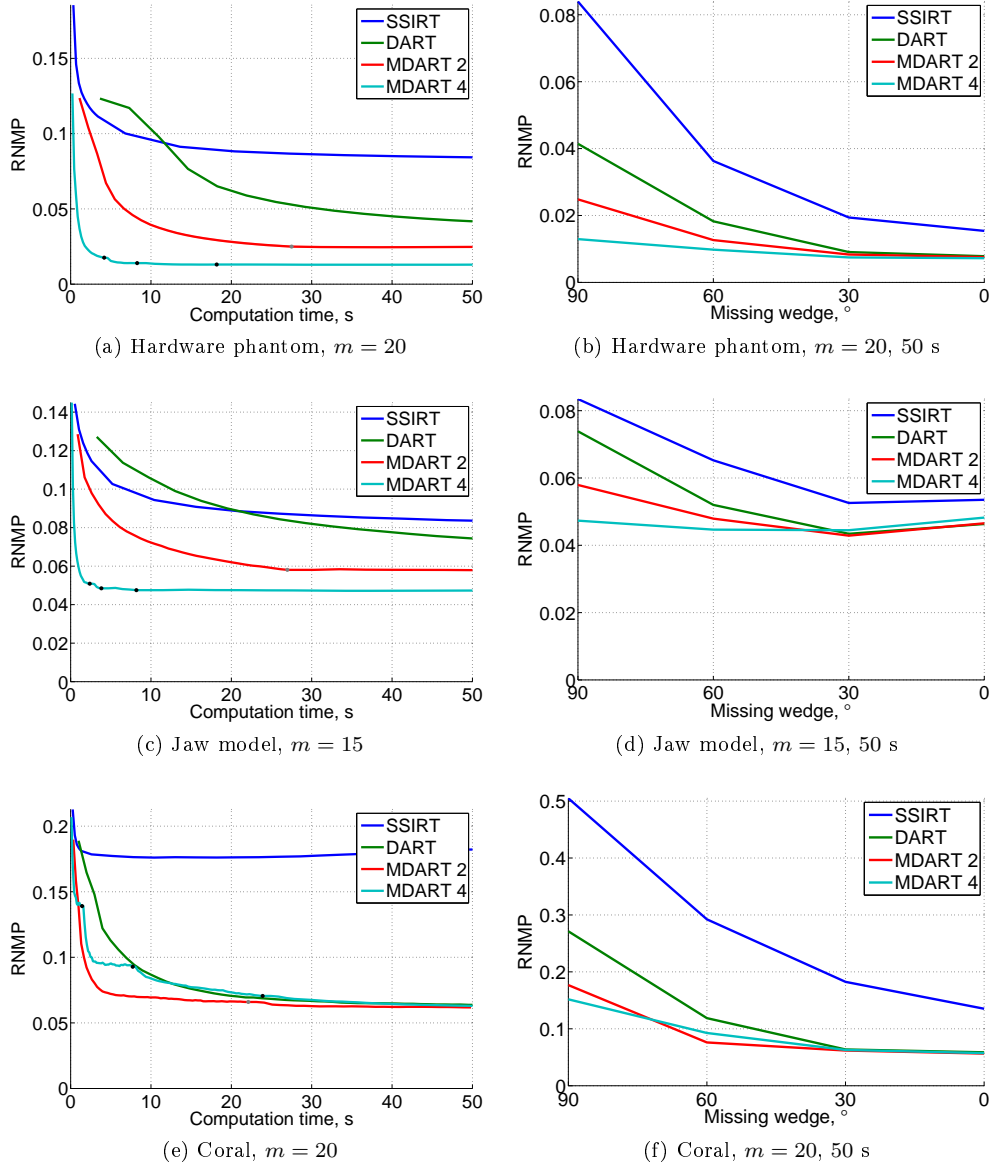


Fig. 13: RNMP for the reconstructions of the real datasets (Fig. 12) as a function of the computation time from the data with the missing wedge (a, c, e) and as a function of the missing wedge after 50 s iteration time (b, d, f). Missing wedge is  $90^{\circ}$  in (a) and (c) and  $30^{\circ}$  in (e). Black and grey points on the MDART curves (a, c, e) mark the moments of switching to a finer reconstruction grid.

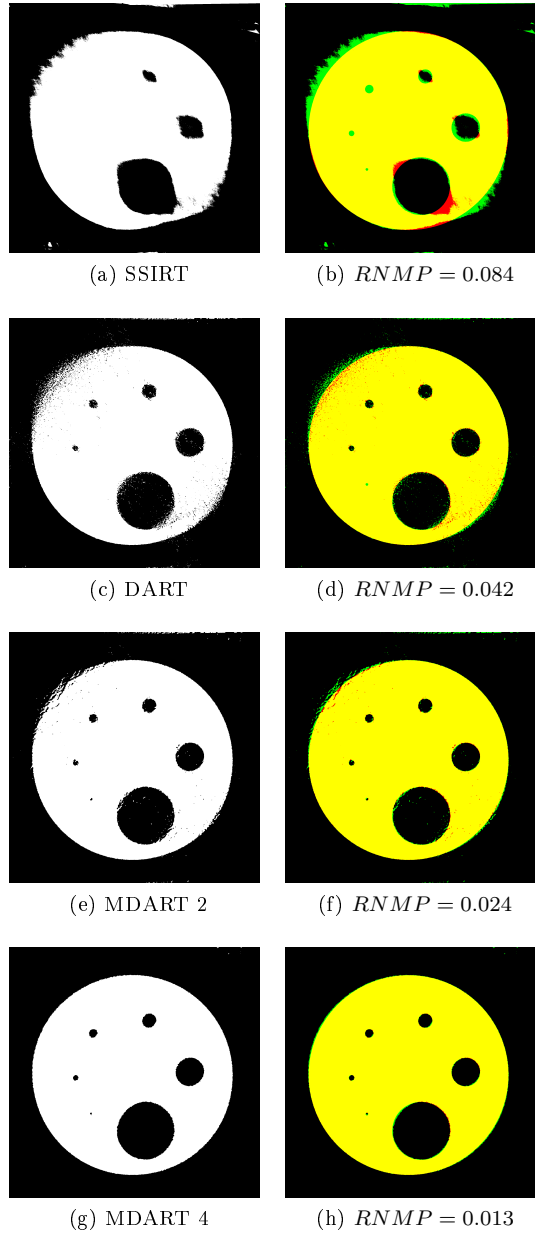


Fig. 14: Reconstructions of the hardware phantom after iterating for 50 s with SSIRT (a), DART (c), MDART 2 (e) and MDART 4 (g) using  $m = 20$  projections with  $90^\circ$  missing wedge together with the corresponding error images (b, d, f, h). Red and green in the error images correspond to misclassified background and object pixels, respectively, black and yellow represent correctly classified background and object pixels, respectively.